

---

This is an electronic reprint of the original article.  
This reprint may differ from the original in pagination and typographic detail.

Antonova, Anna; Eik, Marika; Jokinen, Ville; Puttonen, Jari

## Effect of the roughness of steel fibre surface on its wettability and the cement paste close to fibre surface

*Published in:*  
Construction and Building Materials

*DOI:*  
[10.1016/j.conbuildmat.2021.123139](https://doi.org/10.1016/j.conbuildmat.2021.123139)

Published: 28/06/2021

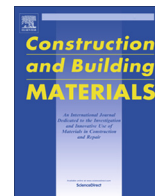
*Document Version*  
Publisher's PDF, also known as Version of record

*Published under the following license:*  
CC BY

*Please cite the original version:*  
Antonova, A., Eik, M., Jokinen, V., & Puttonen, J. (2021). Effect of the roughness of steel fibre surface on its wettability and the cement paste close to fibre surface. *Construction and Building Materials*, 289, Article 123139. <https://doi.org/10.1016/j.conbuildmat.2021.123139>

---

This material is protected by copyright and other intellectual property rights, and duplication or sale of all or part of any of the repository collections is not permitted, except that material may be duplicated by you for your research use or educational purposes in electronic or print form. You must obtain permission for any other use. Electronic or print copies may not be offered, whether for sale or otherwise to anyone who is not an authorised user.



# Effect of the roughness of steel fibre surface on its wettability and the cement paste close to fibre surface



Anna Antonova<sup>a,\*</sup>, Marika Eik<sup>a</sup>, Ville Jokinen<sup>b</sup>, Jari Puttonen<sup>a</sup>

<sup>a</sup> Department of Civil Engineering, Aalto University, Rakentajanaukio 4 A, Otaniemi, 02150 Espoo, Finland

<sup>b</sup> Department of Chemistry and Materials Science, Aalto University, Tietotie 3, Otaniemi, 02150 Espoo, Finland

## HIGHLIGHTS

- Hysteresis increased along with the fibre surface roughness.
- The number of large pores was higher near the smooth fibres than near the rough ones.
- Porosity close to the fibre decreased as the fibre roughness increased.
- Width of the boundary zone was affected by the roughness of the fibre surface.

## ARTICLE INFO

### Article history:

Received 23 December 2020

Received in revised form 16 March 2021

Accepted 18 March 2021

### Keywords:

Fibre–matrix interface

Steel fibre

Surface treatment

k-means clustering

Roughness

Contact angle

Wetting

ITZ

## ABSTRACT

This study experimentally examines the relationship between fibre surface roughness, its wettability, and the microstructure of the cement paste close to the fibre. Results indicate that the amount of water that adheres to or is retained by the fibre surface grows with the increase in roughness. The distributions of porosity and of unhydrated cement grains, which were produced through analysis of BSE images with a k-means clustering algorithm up to 100  $\mu\text{m}$  from fibre surface, revealed a decrease in both large pores and porosity when roughness increased but not a clear effect on the distribution of unhydrated cement grains.

© 2021 The Author(s). Published by Elsevier Ltd. This is an open access article under the CC BY license (<http://creativecommons.org/licenses/by/4.0/>).

## 1. Introduction

The load-bearing capacity of fibre reinforced cementitious (FRC) composites depends upon the microstructure of the fibre–matrix interface that is created through interaction between the fibre surface and the cement paste that surrounds it. The surface of steel fibre provides nucleation sites that enable the hydration reactions and adhesion that bonds the resulting cementitious compounds to the fibre. Cementitious matrix that is formed near the fibre surface is called the interfacial transition zone (ITZ). Extending to about 60  $\mu\text{m}$  from the fibre surface [1], it has a complex and porous microstructure, that differs from that of the bulk cement paste [2,3,1]. ITZ is a weaker region between the fibre and the bulk

cement paste that determines the strength of the bond between them. To ensure efficient bonding, it is important to enhance fibre–matrix interaction.

The surface of fibres can be modified mechanically or chemically to improve the bond. Several studies have examined chemical treatment of steel fibre surface, including zinc phosphate (ZnPh) deposition [4,5], oxygen and argon plasma treatment [6], tetraethoxysilane (TEOS) [7], calcium carbonate ( $\text{CaCO}_3$ ) [8] and nano- $\text{SiO}_2$  coatings [9]. In addition to chemical reactivity, the TEOS and ZnPh depositions created a rough topography on the fibre surface that could improve adhesion between the steel fibre and the cementitious matrix. The authors in [8] observed that the changes in the morphology and size of  $\text{CaCO}_3$  precipitations affected the capacity of the bond between the steel fibre and the ultra-high-performance concrete (UHPC) to the uniaxial loading.

The mechanical modification of steel fibres with sandpaper was recently adopted in [10,11] to study the effect of fibre roughness on

\* Corresponding author.

E-mail addresses: [anna.antonova@aalto.fi](mailto:anna.antonova@aalto.fi) (A. Antonova), [marika.eik@aalto.fi](mailto:marika.eik@aalto.fi) (M. Eik), [ville.p.jokinen@aalto.fi](mailto:ville.p.jokinen@aalto.fi) (V. Jokinen), [jari.puttonen@aalto.fi](mailto:jari.puttonen@aalto.fi) (J. Puttonen).

the capacity of UHPC. The loading tests conducted by both of the studies concluded that sanding the fibre increased the bonding area at the interface and improved both the strength of the fibre–matrix bond and its resistance to the loading. Chung et al. [10] reported that the roughening of the fibre led to an increase of 31–66% in the bond strength. Kim et al. [8] roughened the surface of plain steel fibres with ethylenediaminetetraacetic (EDTA) solution, which increased the capacity of the fibre–matrix bond by more than 80%. The EDTA solution was also used in [12] to modify the surface roughness of steel fibres with circular, triangular and twisted triangular cross-sections. The authors concluded that with the UHPC studied roughening the surfaces of circular and triangular fibres increased the energy required for fibre–matrix debonding by 26 and 39%, respectively, and their tensile strength by 17–26 and 20–36%, respectively. In terms of the twisted triangular fibres, the surface roughening increased the capacity of the fibre–matrix bond, but not so much as twisting reduced it. The microstructure of the fibre–matrix interface was not evaluated in these studies.

The wetting properties of a steel fibre surface can be important to the mixing and setting of fresh concrete mass. The effect of surface roughness on wetting properties was first highlighted by Wenzel [13] and Cassie and Baxter [14]. The recent research reported in [15] demonstrated the influence of surface roughness on the wettability of steel and copper. In [16], the authors explained that the pinning of the water droplet, which is caused by topographical irregularities of the surface, leads to the elongation of the droplet and changes its sliding behaviour. The study introduced in [17], examined the effects of fibre material, roughness, and wettability on the properties of the interface between the geopolymer binder based on fly-ash and the steel and polypropylene fibres. Based on their results, the authors concluded that rough fibre surface exhibited a more hydrophilic behaviour, which resulted in a growth of the bond strength between the fibres and the binder.

Fibre roughness may also affect the spreading and sticking of water along the fibre surface. Xu et al. [18] noted that the formation of water film on the fibre surface during the mixing of concrete is critical to the development of a cementitious matrix close to the fibre surface. Eik et al. [19] and Qudoos et al. [20] discussed the influence of the surface roughness of inclusions, such as fibres and aggregates, on the wettability and on the microstructure of the cement paste near the inclusions. However, studies of the roughness of steel fibre and its effect on fibre–matrix microstructure and bond are quite limited.

The interaction between fibres and cementitious matrix on a micro-scale is the basis for their behaviour in structural members. The present study focused on the influence of the fibre roughness on its surface wetting and the formation of the ITZ around the steel fibre. The results are expected to enhance the understanding of the micro-scale properties of the fibre surface for the development of bonding and debonding between fibres and cement paste. One target of this study was to investigate the connection between the roughness characteristics of fibre surface and its wetting behaviour, which was achieved through contact angle goniometry using the meniscus and sessile droplet methods. The atomic force microscope (AFM) and stylus profilometer, both of which are direct measuring techniques, were used for quantitative evaluation of roughness profiles. The other goal of this study was to investigate if the roughness of fibre surface affects the cement paste within the ITZ. Therefore, the distributions of pores and unhydrated (UH) cement grains were evaluated using a scanning electron microscope (SEM) and image analysis.

## 2. Materials and methods

### 2.1. Materials

Steel fibres (Arcelor Mittal HE 1/50) with a diameter of 1 mm and a length of 40 mm, after cutting the hooks, were examined (Fig. 2) and denoted according to the methods used to process their surfaces. The dash between the name of the treatment process and its notation as follows: electrolytically polished - R1; non-processed - R2; and sanded - R3 (Fig. 1).

Cement paste samples were prepared with ordinary Portland cement (CEM I 52,5N), a water-to-cement ratio of 0.5, and one steel fibre in the middle of each sample. The chemical composition of cement is represented in Table 1. The cement paste prisms were cast in rectangular metal moulds where the steel fibres were fixed vertically in the plywood on the bottom of the mould, Fig. 2. After 24 h, the cement paste prisms were demoulded and cured in the water for the next 27 days. Then the cement paste cylinders with a diameter of 15 mm and a fibre in the middle were drilled out from these prisms and cut with a low-speed diamond saw into 2 parts as demonstrated in Fig. 2. One of the parts received was impregnated in the epoxy resin following the recommendations reported in [22]. The grinding and polishing were performed as proposed in [19]. An example of a sample used in SEM analysis is illustrated in Fig. 2. Cement paste samples were denoted according to the labels of the embedded fibres: R1, R2, and R3.

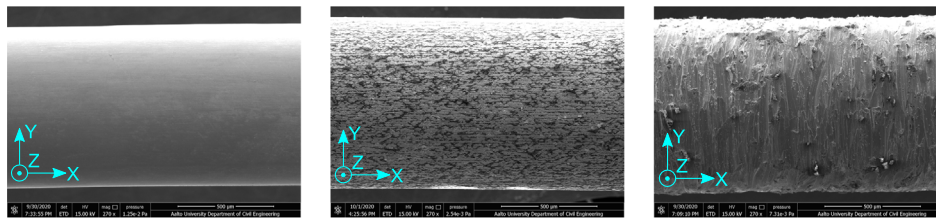
### 2.2. Modification of the steel fibre surface

Electrolytic polishing smooths the fibre surface through oxidation, which enables the removal of iron ions. These ions dissolve more quickly from the peaks than they do from the valleys of the surface profile, and their dissolution flattens the surface in the process. Each steel fibre was fixed in the tweezers and immersed 30 times for 8 s into a 1:3 solution of nitric acid and ethanol at  $-30^{\circ}\text{C}$  under 20 V of electric current (Fig. 3(a), (b)). The fibre was cleaned with ethanol between immersions to remove any iron oxides residue (Fig. 3(a)).

Sandpaper with a grid size of  $60\ \mu\text{m}$  was fixed to the flat vertical surface and used to increase fibre roughness (Fig. 3(c)). The fibre was pressed manually against the sandpaper and dragged back and forth along it (Fig. 3(c)). After six repetitions, the fibre was turned  $90^{\circ}$  and the dragging procedure was repeated. These two sanding steps were done at least 4 times, and an optical microscope was used to check the increase of roughness.

### 2.3. Quantification of fibre surface roughness

An AFM (Bruker Dimension Icon) with a silicon tip on the cantilever (ScanAsyst-Air) and a stylus profilometer (Veeco Dektak 6M) were used to measure the roughness of fibres with different processing of the surface because both provide direct information about the roughness without any need for additional data processing operations. The AFM was used to quantify the roughness of the R1 and R2 fibres. Two areas of  $80 \times 80\ \mu\text{m}^2$  were measured from two locations on three R1 and R2 fibres (Fig. 4). Within each of these areas, 256 lines were scanned in the longitudinal direction of the fibre at a rate of 0.3 Hz. The curvature of fibre in the direction of angular coordinate was considered by mapping the lines measured onto the tangent plane. The mapping was carried out by Nanoscope analysis software.



(a) R1-Polished. (b) R2-Non-processed. (c) R3-Sanded.

Fig. 1. Secondary electron images of the steel fibres with different degrees of surface roughness.

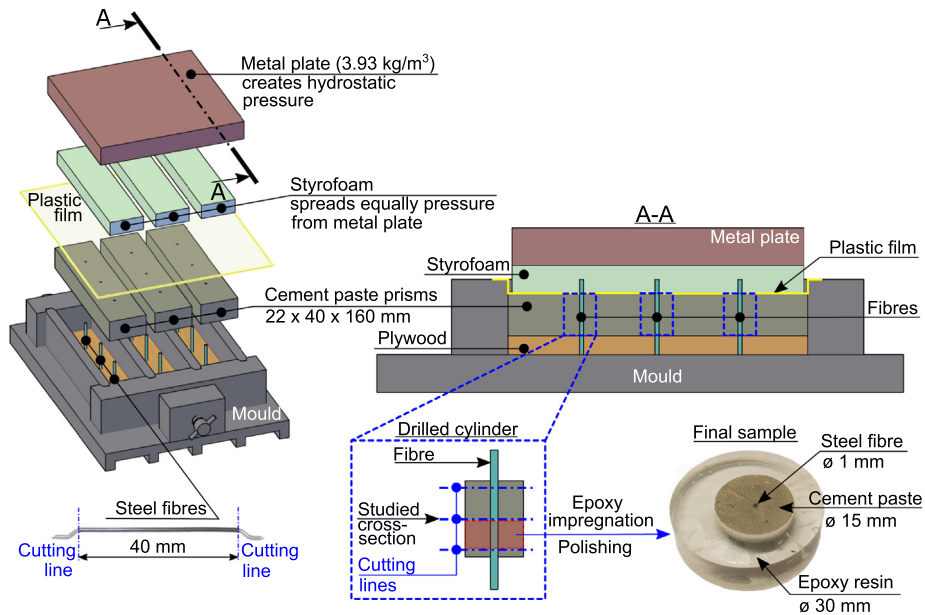
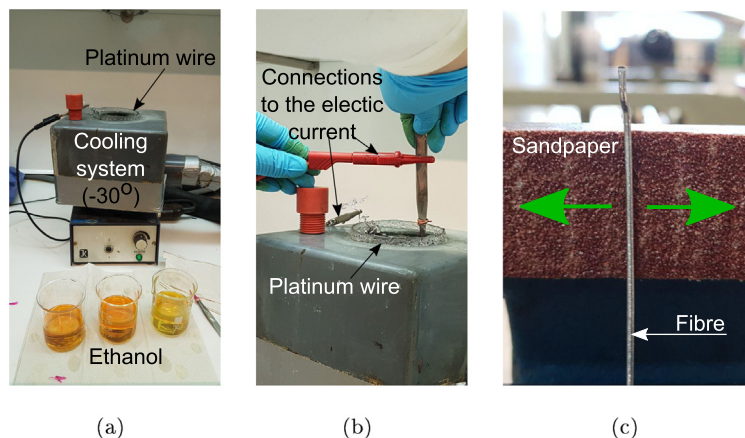


Fig. 2. Preparation of samples for SEM investigation.

Table 1  
Chemical composition of cement.

| Oxides (%) | CaO  | SiO <sub>2</sub> | Al <sub>2</sub> O <sub>3</sub> | Fe <sub>2</sub> O <sub>3</sub> | MgO | SO <sub>3</sub> | Other |
|------------|------|------------------|--------------------------------|--------------------------------|-----|-----------------|-------|
| Clinker1   | 61.5 | 18.5             | 5.1                            | 3.2                            | 4.4 | 2.8             | < 5   |

[1] According to the information provided by the manufacturer [21].



(a) (b) (c)

Fig. 3. (a) Setup for electrolytic polishing. (b) Immersion of fibre into the solution under electric current. (c) Sanding of fibre surface. Green arrows show the directions of fibre movements along the sandpaper. (For interpretation of the references to color in this figure legend, the reader is referred to the web version of this article.)

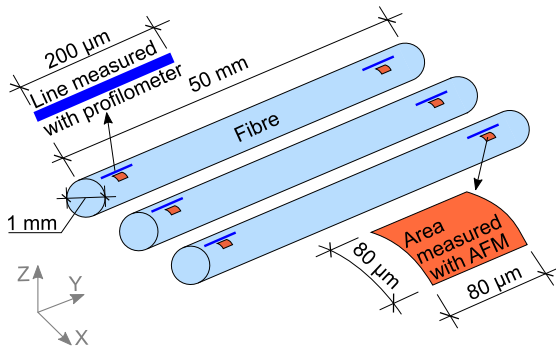


Fig. 4. Locations of the areas scanned with AFM and the lines scanned with stylus profilometer.

The stylus profilometer was used to quantify the roughness of R3 fibres that exceeded the measuring limits of AFM. The stylus profilometer enabled measurement of the surface profile of the steel fibre as a line along its length (X-axis in Fig. 1(c)). To estimate the roughness of the R3 fibres, two lines of 200 µm were measured from two locations on three R3 fibres (Fig. 4).

2.4. Measuring water contact angles on the fibre surface

The wetting properties of steel fibres with different degrees of surface roughness were estimated through contact angle goniometry (Theta, Biolin Scientific). The value of the contact angle of a water droplet on the surface may vary between advancing and receding contact angles, as was explained in [23,24]. An advancing contact angle ( $\theta_a$ ) indicates the water spreading along a dry surface and represents the maximum possible contact angle. A receding contact angle ( $\theta_r$ ) indicates the ability of water to stick to a wet surface and represents the smallest possible contact angle. The lower the receding angle, the better the adhesion of water to the surface.

The advancing angles were measured with a sessile droplet method, starting with a droplet volume of 1 µl and increasing the volume up to 2.5 µl at a rate of 0.1 µl/s (Fig. 5(a)). The size of the water droplets used in this test should be orders of magnitude larger than the size of the surface roughness, ideally by three orders of magnitude [25].

For the measurement of receding angles, two methods were utilized, sessile droplet (Fig. 5(a)) and meniscus (Fig. 5(c)). The method was selected based on the roughness of the fibres and on the range of angles that could accurately be measured. The sessile droplet method only works for reasonably large receding angles, such as those observed on the R1 fibres. The droplet volume was reduced from 2.5 µl down to 0 µl at a rate of 0.1 µl/s (Fig. 5(b)). In the case of the R2 and R3 fibres, the sessile droplet test was not reliable, as the droplet started to recede only at a very low

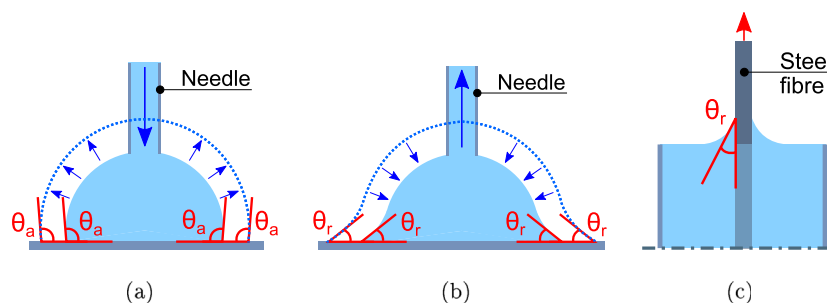


Fig. 5. Scheme of the sessile droplet method: (a) Advancing angle measurement. (b) Receding angle measurement on R1 fibre. (c) Scheme of the meniscus method: Receding angle measurement on R2 and R3 fibres.

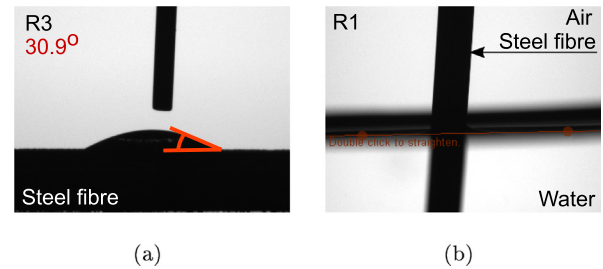


Fig. 6. Limitations of measuring the receding angle (a) with the sessile droplet test on R3 fibre and (b) with the meniscus method on R1 fibre.

volume when its adhesion to the needle was heavily distorted and the receding angles were too small to be measured correctly (Fig. 6(a)). The meniscus method, which best captures reasonably small receding angles, was used for the R2 and R3 fibres (Fig. 5 (c)). These fibres were lowered into a cuvette containing water and lifted at a rate of 10 mm/min in order to achieve a steady receding angle. Due to line-of-sight interference by the water surface, the meniscus method could not capture the large receding angle of the R1 fibres (Fig. 6(b)).

The difference between  $\theta_a$  and  $\theta_r$  is denoted as contact angle hysteresis, which is an important parameter for the evaluation of water droplet mobility on the steel fibre surface. The smaller the hysteresis, the more mobile the droplet [26]. In addition, Marmur et al. in [23] noted that an increase in hysteresis also increases the strength of water attachment to the surface.

2.5. Characterisation of porosity and UH cement grains near the fibre

2.5.1. SEM analysis

SEM Quanta 450 FEG and a backscattered electron (BSE) detector were used to analyse the microstructure of the cement paste close to steel fibres with different degree of surface roughness. BSE images with a magnification of 2300 and resolution of 1px equals 0.117 µm were obtained by operating at 15 kV and at a working distance of 10 mm. The interface between steel fibre and cement paste was captured with 16 BSE images per sample, as demonstrated in Fig. 7. A 100 µm band of hardened cement paste was captured with each BSE image, that assured the coverage of the ITZ with the thickness of around 70 µm reported in the previous studies, as for example in [27,28,1].

The pores and UH cement grains were identified in the BSE images based on their gray-level intensities. The UH cement grains appear brighter than other cementitious phases because of higher atomic numbers of their chemical components [29,30]. On the other hand, pores are empty spaces filled with epoxy resin, which consists mainly of carbon and hydrogen with low atomic numbers.

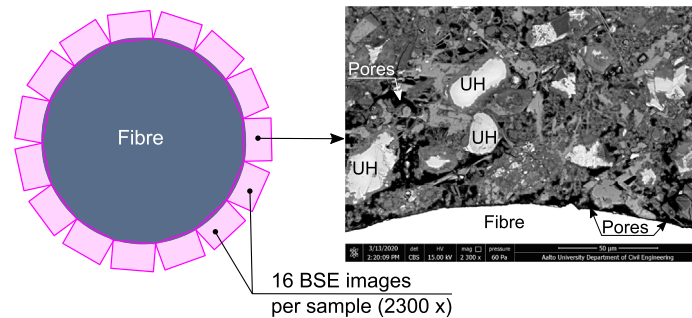


Fig. 7. Locations of the BSE images used to study the fibre–matrix interface per each sample (left). Example of the BSE image (right).

Therefore, pores appear as the darkest regions on the BSE images (Fig. 7).

The bulk cement paste was also analysed through 50 images at the same resolution and magnification in order to identify the area fractions of pores and the UH cement grains that indicate the stabilisation of the cement paste. This analysis also enabled estimation of the boundary effect that was created by fibres with different degrees of surface roughness.

### 2.5.2. Image segmentation

The global thresholding method is widely used for the segmentation of gray-level BSE images of cementitious materials, as in [31–34,1]. The shortcoming of this method is the complexity involved in defining the threshold boundaries unambiguously when the gray-level histogram has no distinct peaks. The authors in [35] introduced the image segmentation of concrete with a mean-shifts (MS) clustering algorithm to study the porosity of the ITZ near a steel bar. The k-means clustering algorithm, which is used for image segmentation in medical [36], biological [37], and other fields [38] can also be used for segmentation of BSE images of cement paste.

In the present study, both the k-means and the MS clustering algorithms were applied on the BSE images of cement paste close to the steel fibre to examine the segmentation efficiency of each method. The library reported in [39] was used for image segmentation. Fig. 8 illustrates the outcomes of the segmentation of BSE image employing both clustering methods. The MS clustering algorithm segmented UH cement grains as heterogeneous phases and over-estimated their number by segmenting some of the hydration products as UH cement grains (Fig. 8(c)). From the material point of view, this uncertainty can be explained by the variation of the gray-level intensities within the cement grains that can be composed of several clinker phases that have different chemical compositions [35,29]. The MS clustering assumes the number of clusters based on the density distribution of the gray-level intensities, meaning that the identification of peaks and valleys of a smooth distribution function is more difficult for the algorithm. Depending on the BSE image segmented, the number of clusters defined by MS clustering varied between 3 and 6. In the case of the k-means clustering, the number of clusters was estimated based on the clustering error, which is the sum of squared Euclidean distances of each data point to its closest clustering centre. According to Fig. 8, a reasonable accuracy of the image segmentation can be achieved with 5 clusters, that corresponds to the value of the clustering error which is not changing any more with the further increase in the number of clusters. As a result, the k-means clustering algorithm recognized UH cement grains as homogeneous phases without over-estimation of their amount (Fig. 8(d)).

The segmented images of pores and UH cement grains were divided into 20 stripes with a width of 5 µm, as demonstrated in

Fig. 9. The ratio of the area of segmented phases in each stripe to the total area of the stripe was calculated in order to define the fraction of segmented phases from the fibre surface. This method, also called the strip delineation method, was used previously in [40,41].

## 3. Results

### 3.1. Roughness of the fibre surface

The roughness profile of the fibre surface was quantified using the X and Z coordinates. Examples of the measured R1, R2, and R3 surface profiles are illustrated in Fig. 10(a)–(c). The roughness of each fibre surface was determined by calculating the average height ( $h_{av}$ ) and the wavelength ( $l_{av}$ ) of the surface profile with the algorithm reported in [19] (Fig. 10(d)) and the root mean square roughness ( $R_q$ ) that corresponds to the standard deviation of the height distribution. The  $R_q$  values of R1 and R2 fibres were calculated with the Nanoscope analysis software. In the case of R3 fibres,  $R_q$  value was calculated with the Eq. (1), as defined in [42].

$$R_q = \sqrt{\frac{1}{n} \sum_{i=1}^n Z_i^2} \quad (1)$$

where  $n$  is the number of the measured points on the surface, and  $Z_i$  is the surface height at the measured point  $i$  (Fig. 10(d)). The parameters of fibre roughness are demonstrated in Table 2.

The R1 fibre had the smallest and the R3 fibre had the largest average wavelength. The  $l_{av}$  of R1 fibre was 62% shorter than that of R2, and  $l_{av}$  of R2 fibre was 61% shorter than that of R3. The measured  $l_{av}$  of the R3 fibre and the size of the sandpaper grains used to modify the surface matched, which explains the values observed. The average height of different fibre surfaces also increased in a pattern similar to that of  $l_{av}$ . The R1 fibre had an  $h_{av}$  that was 91% smaller than that of the R2 fibre, which had an  $h_{av}$  that was 96% smaller than that of the R3 fibre. The  $R_q$  of R1 fibres was 84% smaller than that of R2 fibres, which was 93% smaller than that of the R3 fibres.

### 3.2. Water contact angle measurements on fibre surface

The results of the contact angle measurements and calculation of hysteresis are summarized in Table 3 and illustrated in Fig. 11. The water droplet used for measurement of contact angles had a baseline width ( $BL_d$ ) of more than 1 mm whereas the measured surface roughness of R3 fibres was in 10 µm length scale (Fig. 11 (c)), which is in accordance with a requirement for the sessile droplet test [25].

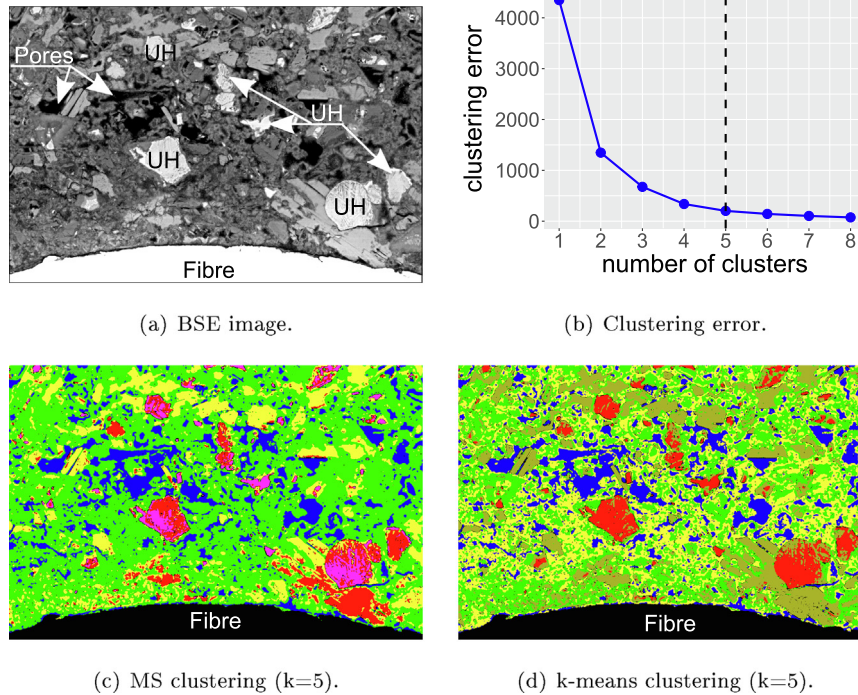


**Fig. 8.** (a) Clustering error as a function of  $k$ . The dashed line marks the reasonable number of clusters. (b–d) Examples of MS and k-means clustering. Pores are marked with blue. UH cement grains are marked with red and magenta. Other hydration products are marked with green, yellow and dark yellow. (For interpretation of the references to color in this figure legend, the reader is referred to the web version of this article.)

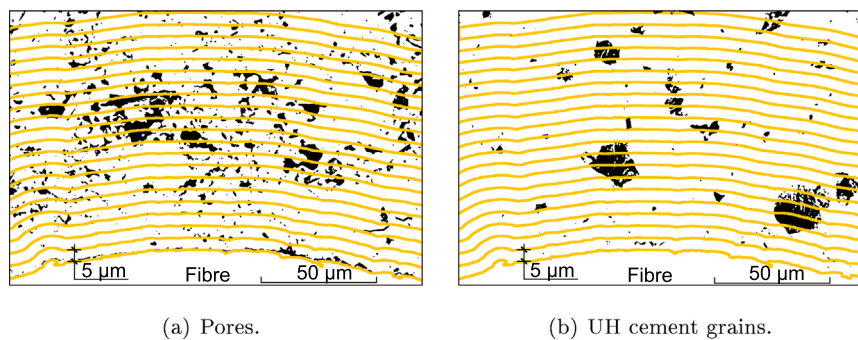


**Fig. 9.** Example of pores and UH cement grains (black regions) segmented from Fig. 8(a). Borders of stripes are marked with yellow lines. (For interpretation of the references to color in this figure legend, the reader is referred to the web version of this article.)

In the advancing contact angle measurement, the edge of the droplet that represents a three-phase (air–liquid–solid) boundary ideally advances equally in all directions, which may not be the case with rough surfaces. The steel fibres studied, have a non-periodic surface roughness. Therefore, the energy needed by the droplet to overcome surface peaks with random heights varies depending on the wetting direction. As the result, the three-phase boundary may encounter a surface peak in one direction, that requires high energy to move forward. Thus, as the volume of the droplet increases, it advances in the direction where the need of energy is the smallest. At the beginning of the advancing process the needle remains in the center of the droplet. However, the position of the needle may shift at a further time-point during the advancing process due to this abrupt movement of the droplet, as demonstrated in Fig. 12b, c. The advancing contact angle in these cases was measured from the advancing side of the droplet. This phenomena appeared on R2 and more strongly on R3 fibres. The advancing angles measured on R2 and R3 fibres represented the averages of the values received with a measuring accuracy of

$\pm 1^\circ$  and  $\pm 3^\circ$ , respectively. The asymmetry observed in terms of water spreading was increasing with the growth of surface roughness. In addition, this asymmetry led also to the slip-stick behaviour of the advancing droplets that was observed on the R3 fibres.

The results demonstrate that the roughness of the fibre surface had a minor effect on the advancing angle and significantly affected the receding angle and hysteresis. The rougher the surface of the fibre, the smaller the receding angle and, thus, the larger the hysteresis. The average receding angle of the R1 fibre was 33% larger than that of the R2. The receding angle of the R2 fibre was 57% larger than the receding angle of the R3 fibre. As a result, the hysteresis of the R3 fibre was 34% larger than the hysteresis of the R2 fibre, which was 26% larger than the hysteresis calculated for the R1 fibre.

### 3.3. Distribution of pores and unhydrated cement grains

The mean distributions of pores and UH cement grains are demonstrated in Fig. 12. In all sample sets, the mean area fraction

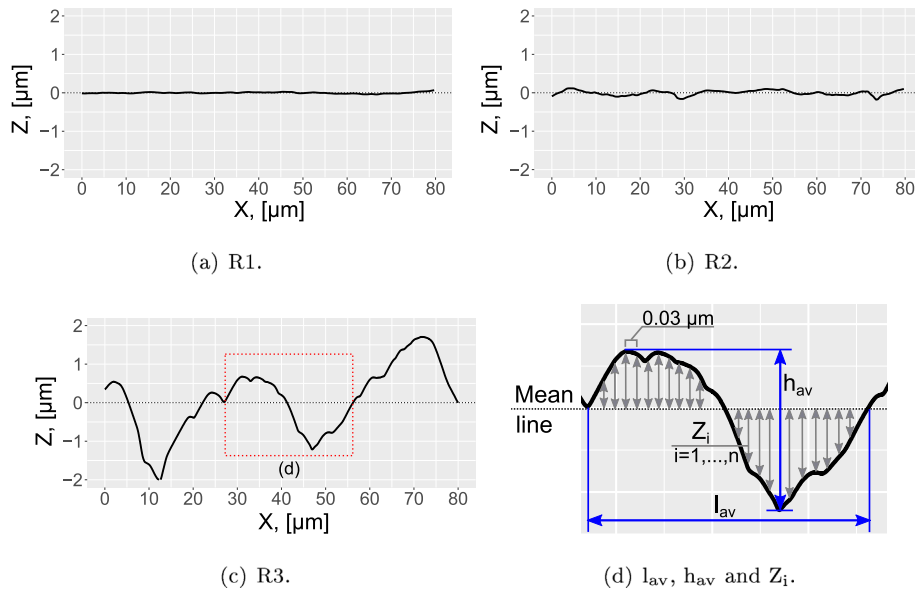


**Fig. 10.** (a–c) Examples of the surface profiles of steel fibres with different degrees of surface roughness. (d) Schematic definition of  $l_{av}$ ,  $h_{av}$  and  $Z_i$ . Each  $Z$  value was measured with the  $0.03 \mu\text{m}$  step.

**Table 2**  
Roughness parameters of different fibre surfaces.

| Fibre surface | $h_{av}$ , $[\mu\text{m}]$ | $l_{av}$ , $[\mu\text{m}]$ | $R_q$ , $[\mu\text{m}]$ |
|---------------|----------------------------|----------------------------|-------------------------|
| R1            | 0.02                       | 8.14                       | 0.031                   |
| R2            | 0.23                       | 21.50                      | 0.191                   |
| R3            | 5.58                       | 55.42                      | 2.667                   |

**Table 3**  
Mean values of  $\theta_a$ ,  $\theta_r$  and hysteresis of fibres with different degrees of surface roughness.

| Fibre surface | $\theta_a$               | $\theta_r$             | Hysteresis               |
|---------------|--------------------------|------------------------|--------------------------|
| R1            | $98.7^\circ \pm 2^\circ$ | $52^\circ \pm 4^\circ$ | $46.7^\circ \pm 6^\circ$ |
| R2            | $97.7^\circ \pm 1^\circ$ | $35^\circ \pm 4^\circ$ | $62.7^\circ \pm 5^\circ$ |
| R3            | $99.2^\circ \pm 3^\circ$ | $15^\circ \pm 2^\circ$ | $84.2^\circ \pm 5^\circ$ |

of pores decreased gradually as the distance from the fibre surface increased. Porosity was lowest close to the R3 fibres, reducing from 27.6 to 8.4%. In the R2 samples, the porosity decreased from 34.1 to 12.6%. The highest porosity was observed close to the R1 fibres, which decreased from 38.2 to 17.8%. On average, the porosity near the R1 fibres was 30% larger than the porosity close to the R2 fibres, which was 33% larger than the porosity near the R3 fibres. According to Fig. 13, the individual distributions of porosities followed the same patterns as the mean lines with only minor fluctuations. The standard deviation of porosity was the largest in the vicinity of the R1 fibres and the lowest near the R3 fibres (Fig. 13). The most evident stabilisation of porosity distribution was noticed at around  $45 \mu\text{m}$  from the R3 fibres in all measured cases and was also close to the mean value of the porosity in the bulk cement paste (equal to  $11.0 \pm 2.0\%$ ; see Figs. 12(a), 13(e)). The linear interpolation of the porosity distributions near the R1 and R2 fibres (dot-dashed lines) showed that a porosity value of around 11.0% could be

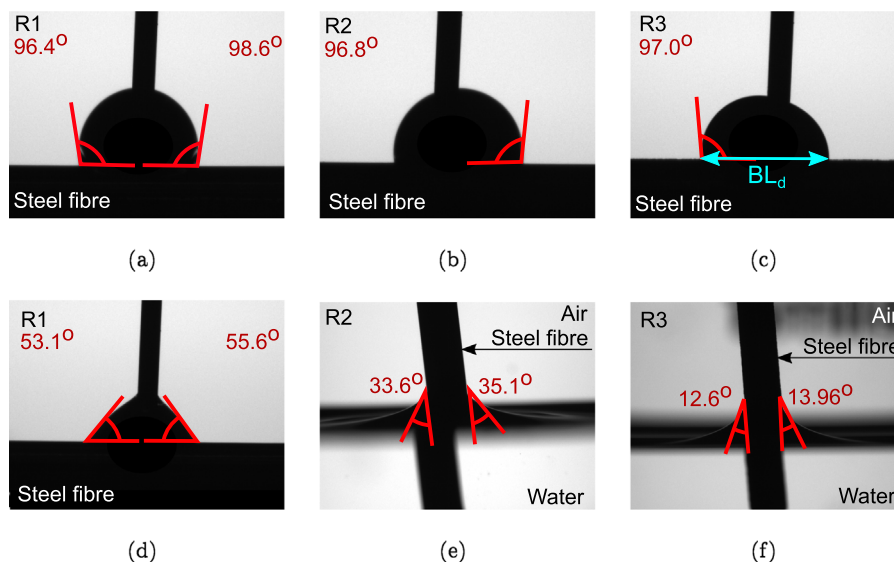
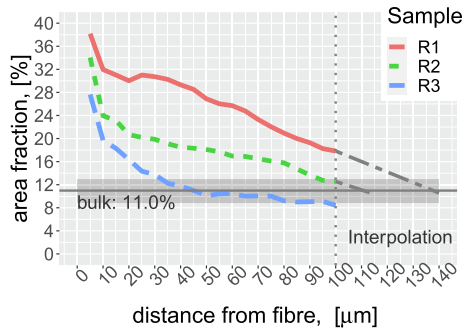
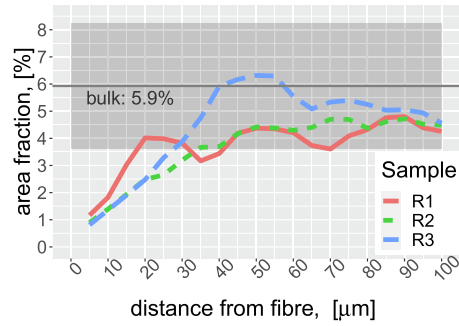


**Fig. 11.** (a–c) Examples of advancing angles measured with the sessile droplet test. (d–f) Examples of receding angle measured on (d) R1 fibre with the sessile droplet test and (e–f) R2 and R3 fibres with the meniscus test.

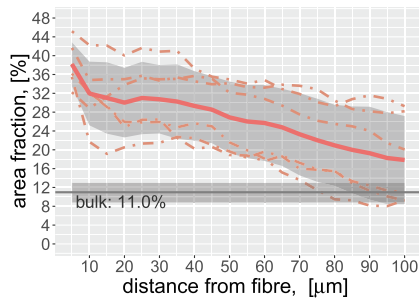


(a) Distribution of pores.

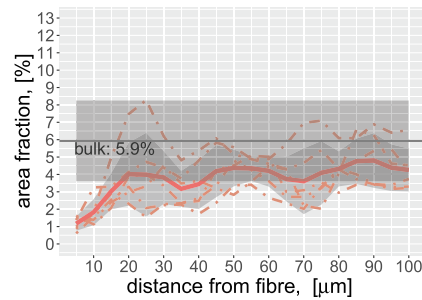


(b) Distribution of UH.

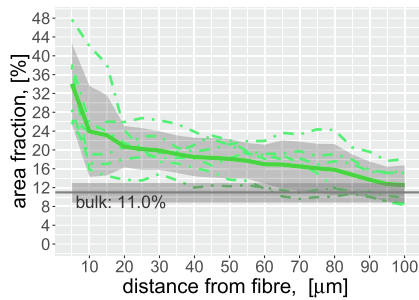
**Fig. 12.** Mean distributions of pores and UH cement grains with the step of 5  $\mu\text{m}$ . Mean area fraction and standard deviation of the corresponding phase in bulk material are marked with gray solid line and gray band, respectively. (For interpretation of the references to color in this figure legend, the reader is referred to the web version of this article.)



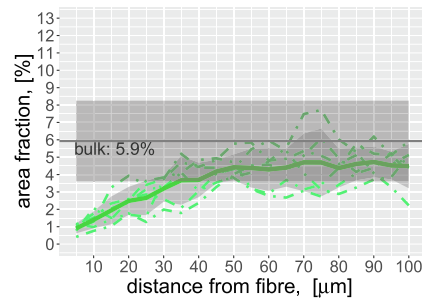
(a) R1. Pores.



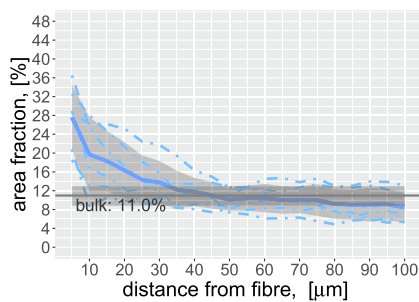
(b) R1. UH cement grains.



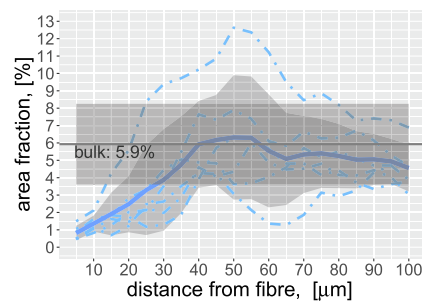
(c) R2. Pores.



(d) R2. UH cement grains.



(e) R3. Pores.



(f) R3. UH cement grains.

**Fig. 13.** Individual (dot-dashed lines) and mean (solid lines) distributions of pores and UH cement grains from the fibre with the standard deviation (gray range). Standard deviation of corresponding phases in bulk material is also marked with gray range. (For interpretation of the references to color in this figure legend, the reader is referred to the web version of this article.)

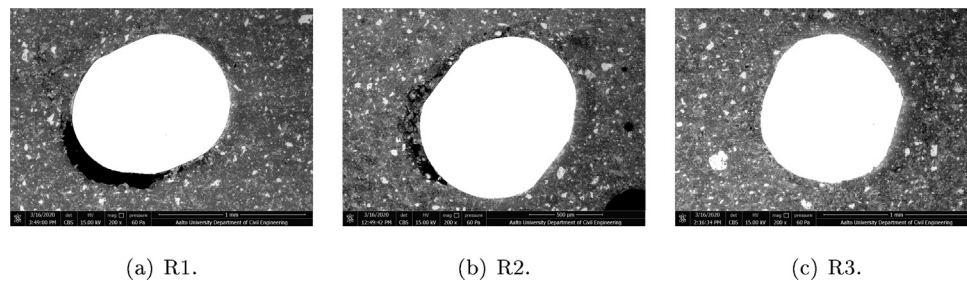


**Fig. 14.** BSE images of steel fibres with different degrees of surface roughness surrounded by the cement paste. Large pores are observed close to the R1 and R2 fibres.

reached in these samples at the distances of  $111\ \mu\text{m}$  and  $138\ \mu\text{m}$ , respectively (Fig. 12(a)).

Large pores in the vicinity of the R1 fibres were noticed in 5 out of 6 samples (Fig. 14(a)). Large pores were observed in 4 out of 6 samples with R2 fibres, though some were loosely occupied with the hydration products (Fig. 14(b)). Cement paste was densely packed close to R3 fibres, as represented in Fig. 14(c), and the large pores were present only in 1 sample.

The mean and individual distributions of UH cement grains as a function of the distance from the fibre surface fluctuated in all of the sample sets (Figs. 12(b), 13). However, the mean area fractions of UH cement grains increased near the R1, R2, and R3 fibres and reached the values of 4.0, 4.4, and 5.9% at distances of 20, 50, and  $40\ \mu\text{m}$ , respectively (Fig. 12b). In the R3 samples, the area fraction of UH cement grains at a distance of  $40\ \mu\text{m}$  equalled the mean value of the UH cement grains in the bulk material ( $5.9 \pm 2.3\%$ ). Then the mean area fraction of UH cement grains increased up to 6.3% at a distance of  $50\ \mu\text{m}$  from the R3 fibres, after which it decreased slightly until reaching the value of 4.6%. After  $20\ \mu\text{m}$  from the R1 and  $50\ \mu\text{m}$  from the R2 fibres, the mean area fractions of UH cement grains fluctuated between 3.2 and 4.8% and between 4.3 and 4.7%, respectively, without reaching the mean value of UH in the bulk material within  $100\ \mu\text{m}$  from the fibre surface.

#### 4. Discussions

The outcomes illustrate the relationship between the roughness and the wettability of the fibre surface and their connection to the formation of the microstructure of the cement paste close to the fibre. The results indicate that the receding angle decreases with the increase of fibre roughness, while the advancing angle is almost independent of the surface roughness (Table 3). Similar behaviour by water droplets was also observed with the other materials, such as glass in [43]. Therefore, the correlation between the roughness of the fibre surface and its wetting properties can be explained by the values of the receding angle. The receding angle decreases on the rough surface due to the clinging of water to the surface irregularities as was explained in [16]. As the hysteresis is the difference between the advancing and receding angles, increased fibre roughness leads to a growth of hysteresis (Table 3), which also indicates the ability of water to retain on the fibre surface [44]. Therefore, it can be assumed that a rough steel fibre surface will extend the surface area covered by water. This change in wetting properties may affect the setting and the hardening of fresh cementitious mass in the vicinity of the fibre. The uniform distribution of water along the fibre surface promotes the hydration of cement grains and results in a more homogeneous microstructure of the cement paste and improved contact with the fibre surface.

Figs. 12(a) and 13 clearly illustrate that the increase in surface roughness decreases porosity near the fibres and their distributions

are distinctly separated. The water close to a smooth fibre surface can gather into large droplets that are localised and unevenly distributed, leading to the formation of large pores as noted in [45]. The SEM analyses show that the number of large pores close to the fibre decreases as the surface roughness increases (Fig. 14). The formation of large pores close to the R1 and R2 fibres demonstrates that the hydration process does not effectively utilise the concentrations of water close to the fibre surface, which was also the outcome in [40], where no hydrates were observed in the locations with increased amounts of water. The number of large pores was also observed to be larger near the hydrophobic polypropylene fibres than in the bulk cement paste in [1].

The decrease of porosity and increase in the number of UH cement grains amongst all fibres regardless of surface roughness indicates the existence of a boundary zone that is similar to that reported in [1,40,46,47] (Fig. 12(a), (b)). In the case of the R3 samples, the mean distributions of pores and UH cement grains approach the mean values of the corresponding phases in the bulk cement paste at a distance of around  $40\ \mu\text{m}$ , which indicates the existence of a denser cement paste microstructure and a narrower boundary zone than near the R1 and R2 fibres. The area fraction of UH cement grains in Fig. 12(b) is the highest up to a distance of  $30\ \mu\text{m}$  from the R1 fibres, which have the lowest surface roughness. The authors in [19] found that the roughness of the fibre surface can indicate the size of the empty spaces available for cement grains, which improves their packaging around the fibres. Similarly, the rough aggregate surfaces examined in [20] were found to result in a better packing of cement grains close to the aggregates. The lower surface roughness of the R1 fibres may have resulted in poor packing of the cement grains and the creation of empty spaces that could not be entirely filled with the hydrates due to the inability of the cement grains to utilise the agglomerated water completely during the hydration. The R3 fibres, on the other hand, have the largest degree of surface roughness, which provides a greater contact area with the cement paste. As a result, the distribution of water along the surface is more uniform. The surface irregularities create empty spaces that enable a better packing of the small cement grains, that can hydrate completely up to the size of  $5 - 7\ \mu\text{m}$  [48,49]. Thereby a dense layer of hydrates can develop around the rough fibres, improving the bond between the fibre and the cement matrix and the efficiency of the final composite. The area fraction of UH cement grains further than  $30\ \mu\text{m}$  from the R3 fibre is larger than the area fraction from the R1 and R2 fibres. This is due to the absence of large pores and to the efficient packing of the cement grains, the size of which can be observed to increase with the distance from the fibre in BSE images by a detectable unhydrated core. In the case of the R1 and R2 fibres, the area fraction of UH cement grains increases up to  $100\ \mu\text{m}$  from the fibres, which means that the packing of the cement grains also improves over a greater distance around these fibres than around the R3 fibre.

## 5. Conclusion

In the present study, the fibre surface roughness was investigated in terms of the wettability of fibre surface and the microstructure of the cement paste close to the fibre surface. The roughness was quantified with AFM and stylus profilometer. The roughness was compared with the fibre wettability measured with contact angle goniometry. The relative amount of pores and UH cement grains around the fibre surfaces with three different roughness profiles were obtained by analysing the SEM images of the ITZ with the k-means clustering algorithm. Based on the results of this study, the following conclusions can be drawn.

- The root mean square roughness ( $R_q$ ) of steel fibres decreased by 84% with the immersion of fibres in nitric acid and ethanol solution under electric current. The initial  $R_q$  of the fibres was 93% smaller than that of the fibres sanded in the perpendicular direction to its axis with the 60  $\mu\text{m}$ -grid sandpaper.
- The contact angle hysteresis decreased 26% by smoothing the fibre and increased 34% by roughening, which also indicated the change in the fibre wetting properties. The increase of fibre roughness added a step-wise nature to the spreading of a water droplet on the fibre surface.
- The fibre surface roughness had a clear effect on the porosity of the cement paste close to the fibre surface. The porosity close to the R1 fibres was the highest being 30% greater than the porosity close to the R2 fibres, where it was 33% more than near the R3 fibres. The SEM analyses indicated that the number of large pores decreased as fibre roughness increased.
- The boundary zone was clearly detected close to R3 fibres, where the distributions of porosity and UH cement grains stabilised at the distance of around 40  $\mu\text{m}$  from the fibre surface. The boundary zone extended more than 100  $\mu\text{m}$  from the surface of the fibres R1 and R2.

This study has demonstrated that the surface topography of a steel fibre can influence the formation of the fibre–matrix interface and should not be neglected in the development of FRC composites.

## CRediT authorship contribution statement

**Anna Antonova:** Conceptualization, Methodology, Formal analysis, Investigation, Writing - original draft, Writing - review & editing, Visualization, Software, Data curation. **Marika Eik:** Conceptualization, Supervision, Writing - review & editing, Software. **Ville Jokinen:** Investigation, Writing - review & editing. **Jari Puttonen:** Conceptualization, Supervision, Writing - review & editing.

## Declaration of Competing Interest

The authors declare that they have no known competing financial interests or personal relationships that could have appeared to influence the work reported in this paper.

## Acknowledgment

This work was supported by the AaltoENG doctoral programme of the School of Engineering of the Aalto University.

## References

- [1] M. Eik, A. Antonova, J. Puttonen, Phase contrast tomography to study near-field effects of polypropylene fibres on hardened cement paste, *Cement and Concrete Composites* (2020), <https://doi.org/10.1016/j.cemconcomp.2020.103800> 103800.
- [2] K.L. Scrivener, A.K. Crumbie, P. Laugesen, The interfacial transition zone (itz) between cement paste and aggregate in concrete, *Interface Science* 12 (4) (2004) 411–421, <https://doi.org/10.1023/B:INTS.0000042339.92990.4c>.
- [3] X.H. Wang, S. Jacobsen, J.Y. He, Z.L. Zhang, S.F. Lee, H.L. Lein, Application of nanoindentation testing to study of the interfacial transition zone in steel fiber reinforced mortar, *Cement and Concrete Research* 39 (8) (2009) 701–715, <https://doi.org/10.1016/j.cemconres.2009.05.002>.
- [4] T. Sugama, N. Carciello, L. Kukacka, G. Gray, Interface between zinc phosphate-deposited steel fibres and cement paste, *Journal of Materials Science* 27 (11) (1992) 2863–2872, <https://doi.org/10.1007/BF01154093>.
- [5] D. Soulioti, N.-M. Barkoula, F. Koutsianopoulos, N. Charalambakis, T. Matikas, The effect of fibre chemical treatment on the steel fibre/cementitious matrix interface, *Construction and Building Materials* 40 (2013) 77–83, <https://doi.org/10.1016/j.conbuildmat.2012.09.111>.
- [6] H.D. Miller, A. Akbarnezhad, S. Mesgari, S.J. Foster, Performance of oxygen/argon plasma-treated steel fibres in cement mortar, *Cement and Concrete Composites* 97 (2019) 24–32, <https://doi.org/10.1016/j.cemconcomp.2018.12.015>.
- [7] C.A. Casagrande, S.H.P. Cavalaro, W.L. Repette, Ultra-high performance fibre-reinforced cementitious composite with steel microfibers functionalized with silane, *Construction and Building Materials* 178 (2018) 495–506, <https://doi.org/10.1016/j.conbuildmat.2018.05.167>.
- [8] S. Kim, S. Choi, D.-Y. Yoo, Surface modification of steel fibers using chemical solutions and their pullout behaviors from ultra-high-performance concrete, *Journal of Building Engineering* 32 (2020), <https://doi.org/10.1016/j.jobe.2020.101709>.
- [9] Z. Pi, H. Xiao, J. Du, M. Liu, H. Li, Interfacial microstructure and bond strength of nano-sio2-coated steel fibers in cement matrix, *Cement and Concrete Composites* 103 (2019) 1–10, <https://doi.org/10.1016/j.cemconcomp.2019.04.025>.
- [10] B. Chun, D.-Y. Yoo, N. Banthia, Achieving slip-hardening behavior of sanded straight steel fibers in ultra-high-performance concrete, *Cement and Concrete Composites* 113 (2020), <https://doi.org/10.1016/j.cemconcomp.2020.103669> 103669.
- [11] D.-Y. Yoo, B. Chun, Enhancing the rate dependent fiber/matrix interfacial resistance of ultra-high-performance cement composites through surface abrasion, *Journal of Materials Research and Technology* 9 (5) (2020) 9813–9823, <https://doi.org/10.1016/j.jmrt.2020.06.080>.
- [12] D.-Y. Yoo, Y.S. Jang, B. Chun, S. Kim, Chelate effect on fiber surface morphology and its benefits on pullout and tensile behaviors of ultra-high-performance concrete, *Cement and Concrete Composites* 115 (2021), <https://doi.org/10.1016/j.cemconcomp.2020.103864> 103864.
- [13] R.N. Wenzel, Resistance of solid surfaces to wetting by water, *Industrial & Engineering Chemistry* 28 (8) (1936) 988–994, <https://doi.org/10.1021/ie50320a024>.
- [14] A.B.D. Cassie, S. Baxter, Wettability of porous surfaces, *Trans. Faraday Soc.* 40 (1944) 546–551, <https://doi.org/10.1039/TF9444000546>.
- [15] K. Kubiak, M. Wilson, T. Mathia, P. Carval, Wettability versus roughness of engineering surfaces, *Wear* 271 (3) (2011) 523–528, <https://doi.org/10.1016/j.wear.2010.03.029>.
- [16] J. Park, S. Kumar, Droplet sliding on an inclined substrate with a topographical defect, *Langmuir* 33 (29) (2017) 7352–7363, <https://doi.org/10.1021/acs.langmuir.7b01716>.
- [17] N. Ranjbar, S. Talebian, M. Mehrali, C. Kuenzel, H.S.C. Metselaar, M.Z. Jumaat, Mechanisms of interfacial bond in steel and polypropylene fiber reinforced geopolymer composites, *Composites Science and Technology* 122 (2016) 73–81, <https://doi.org/10.1016/j.compscitech.2015.11.009>.
- [18] L. Xu, F. Deng, Y. Chi, Nano-mechanical behavior of the interfacial transition zone between steel-polypropylene fiber and cement paste, *Construction and Building Materials* 145 (2017) 619–638, <https://doi.org/10.1016/j.conbuildmat.2017.04.035>.
- [19] M. Eik, A. Antonova, J. Puttonen, Roughness of steel fibre and composition of cement paste close to fibre surface, *Journal of Advanced Concrete Technology* 17 (11) (2019) 628–638, <https://doi.org/10.3151/jact.17.628>.
- [20] A. Qudoos, A. ur Rehman, H.G. Kim, J.-S. Ryou, Influence of the surface roughness of crushed natural aggregates on the microhardness of the interfacial transition zone of concrete with mineral admixtures and polymer latex, *Construction and Building Materials* 168 (2018) 946–957, <https://doi.org/10.1016/j.conbuildmat.2018.02.205>.
- [21] Megasentti: technical data sheet, <http://www.finnsementti.fi> (2019).
- [22] H. Wong, N. Buenfeld, Patch microstructure in cement-based materials: Fact or artefact?, *Cement and Concrete Research* 36 (5) (2006) 990–997, <https://doi.org/10.1016/j.cemconres.2006.02.008>.

- [23] A. Marmur, C. Della Volpe, S. Siboni, A. Amirfazli, J.W. Drelich, Contact angles and wettability: towards common and accurate terminology, *Surface, Innovations* 5 (1) (2017) 3–8, <https://doi.org/10.1680/jsuin.17.00002>.
- [24] J.W. Drelich, Contact angles: From past mistakes to new developments through liquid-solid adhesion measurements, *Advances in Colloid and Interface Science* 267 (2019) 1–14, <https://doi.org/10.1016/j.cis.2019.02.002>.
- [25] A. Marmur, Solid-surface characterization by wetting, *Annual Review of Materials Research* 39 (1) (2009) 473–489, <https://doi.org/10.1146/annurev.matsci.38.060407.132425>.
- [26] T. Huhtamäki, X. Tian, J.T. Korhonen, R.H. Ras, Surface-wetting characterization using contact-angle measurements, *Nature Protocols* 13 (7) (2018) 1521–1538, <https://doi.org/10.1038/s41596-018-0003-z>.
- [27] A. Leemann, B. Münch, P. Gasser, L. Holzer, Influence of compaction on the interfacial transition zone and the permeability of concrete, *Cement and Concrete Research* 36 (8) (2006) 1425–1433, <https://doi.org/10.1016/j.cemconres.2006.02.010>.
- [28] Y. Shao, Z. Li, S.P. Shah, Matrix cracking and interface debonding in fiber-reinforced cement-matrix composites, *Advanced Cement Based Materials* 1 (2) (1993) 55–66, [https://doi.org/10.1016/1065-7355\(93\)90010-L](https://doi.org/10.1016/1065-7355(93)90010-L).
- [29] S. Diamond, The microstructure of cement paste and concrete a visual primer, *Cement and Concrete Composites* 26 (8) (2004) 919–933, <https://doi.org/10.1016/j.cemconcomp.2004.02.028>.
- [30] K.L. Scrivener, Backscattered electron imaging of cementitious microstructures: understanding and quantification, *Cement and Concrete Composites* 26 (8) (2004) 935–945, <https://doi.org/10.1016/j.cemconcomp.2004.02.029>.
- [31] K.L. Scrivener, H.H. Patel, P.L. Pratt, L.J. Parrott, Analysis of phases in cement paste using backscattered electron images, methanol adsorption and thermogravimetric analysis, *MRS Proceedings* 85 (1986) 67, <https://doi.org/10.1557/PROC-85-67>.
- [32] H. Wong, M. Head, N. Buenfeld, Pore segmentation of cement-based materials from backscattered electron images, *Cement and Concrete Research* 36 (6) (2006) 1083–1090, <https://doi.org/10.1016/j.cemconres.2005.10.006>.
- [33] H.S. Wong, K. Matter, N.R. Buenfeld, Estimating the original cement content and water cement ratio of portland cement concrete and mortar using backscattered electron microscopy, *Magazine of Concrete Research* 65 (11) (2013) 693–706, <https://doi.org/10.1680/macr.12.00201>.
- [34] D.P. Bentz, P.E. Stutzman, Curing, hydration, and microstructure of cement paste, *ACI Materials Journal* 103 (5) (2006) 348, <https://doi.org/10.14359/18157>.
- [35] A. Kenny, A. Katz, Characterization of the interfacial transition zone around steel rebar by means of the mean shift method, *Materials and Structures* 45 (5) (2012) 639–652, <https://doi.org/10.1617/s11527-011-9786-x>.
- [36] H. Mofteh, A. Azar, E. Al-Shammari, N. Ghali, A.E. Hassanien, M. Shoman, Adaptive k-means clustering algorithm for mr breast image segmentation, *Neural Computing and Applications* 24 (2013), <https://doi.org/10.1007/s00521-013-1437-4>.
- [37] H. Yao, Q. Duan, D. Li, J. Wang, An improved k-means clustering algorithm for fish image segmentation, *Mathematical and Computer Modelling* 58 (3) (2013) 790–798, <https://doi.org/10.1016/j.mcm.2012.12.025>.
- [38] M. Mohd, S. Herman, Z. Sharif, Application of k-means clustering in hot spot detection for thermal infrared images (2017) 107–110, <https://doi.org/10.1109/ISCAIE.2017.8074959>.
- [39] F. Pedregosa, G. Varoquaux, A. Gramfort, V. Michel, B. Thirion, O. Grisel, M. Blondel, P. Prettenhofer, R. Weiss, V. Dubourg, J. Vanderplas, A. Passos, D. Cournapeau, M. Brucher, M. Perrot, E. Duchesnay, Scikit-learn: Machine learning in Python, *Journal of Machine Learning Research* 12 (2011) 2825–2830.
- [40] A. Horne, I. Richardson, R. Brydson, Quantitative analysis of the microstructure of interfaces in steel reinforced concrete, *Cement and Concrete Research* 37 (12) (2007) 1613–1623, <https://doi.org/10.1016/j.cemconres.2007.08.026>.
- [41] Y. Gao, G.D. Schutter, G. Ye, H. Huang, Z. Tan, K. Wu, Porosity characterization of itz in cementitious composites: Concentric expansion and overflow criterion, *Construction and Building Materials* 38 (2013) 1051–1057, <https://doi.org/10.1016/j.conbuildmat.2012.09.047>.
- [42] Geometrical Product Specifications (GPS) – Surface texture: Profile method – Terms, definitions and surface texture parameters, Standard, International Organization for Standardization, Geneva, CH (apr 1997)..
- [43] S. Semal, T.D. Blake, V. Geskin, M.J. de Ruijter, G. Castelein, J. De Coninck, Influence of surface roughness on wetting dynamics, *Langmuir* 15 (25) (1999) 8765–8770, <https://doi.org/10.1021/la980539z>.
- [44] C.W. Extrand, Y. Kumagai, Liquid drops on an inclined plane: The relation between contact angles, drop shape, and retentive force, *Journal of Colloid and Interface Science* 170 (2) (1995) 515–521, <https://doi.org/10.1006/jcis.1995.1130>.
- [45] J.P. Hwang, M. Kim, K.Y. Ann, Porosity generation arising from steel fibre in concrete, *Construction and Building Materials* 94 (2015) 433–436, <https://doi.org/10.1016/j.conbuildmat.2015.07.044>.
- [46] H. Wong, N. Buenfeld, Euclidean distance mapping for computing microstructural gradients at interfaces in composite materials, *Cement and Concrete Research* 36 (6) (2006) 1091–1097, <https://doi.org/10.1016/j.cemconres.2005.10.003>.
- [47] K.L. Scrivener, A. Bentur, P.L. Pratt, Quantitative characterization of the transition zone in high strength concretes, *Advances in Cement Research* 1 (4) (1988) 230–237, <https://doi.org/10.1680/adcr.1988.1.4.230>.
- [48] K.O. Kjellsen, H. Justnes, Revisiting the microstructure of hydrated tricalcium silicate – a comparison to portland cement, *Cement and Concrete Composites* 26 (8) (2004) 947–956, scanning electron microscopy of cements and concretes. doi: 10.1016/j.cemconcomp.2004.02.030.
- [49] K.L. Scrivener, The development of microstructure during the hydration of portland cement. (1984)..